Journal of Inorganic and Organometallic Polymers and Materials (2020) 30:4129–4141
https://doi.org/10.1007/s10904-020-01563-0

Ternary CdS/MoS_2/ZnO Photocatalyst: Synthesis, Characterization and Degradation of Ofloxacin Under Visible Light Irradiation

Ali İmran Vaizoğullar[1]

Received: 26 March 2020 / Accepted: 25 April 2020 / Published online: 4 May 2020

Abstract
Ternary CdS/MoS_2/ZnO (CMZ) photocatalyst was prepared that successfully degraded ofloxacin antibiotic under visible light irradiation. SEM mapping analyses of CMZ showed homogenous elemental distribution. The XRD analysis shows that ternary composites contained ZnO in the hexagonal wurtzite, CdS in cubic phase and MoS_2 in the hexagonal structure. UV-DRS results of CMZ exhibited thresholds of ~ 430 nm. The photocatalytic degradation studies were performed with ofloxacin antibiotic (290 nm) under visible light irradiation. BET results presented Type III isotherm and H3 hysteresis. Ternary CMZ showed higher photoelectrochemical and photocatalyic activity due to prolonged lifetime of charge it carries, crystalline defect and surface plasmon resonance of CdS. The kinetic rate constant of ternary CMZ was 4 times higher than that of CdS/MoS_2 (CM). This study presents an effective photocatalysis and the mechanism of ofloxacin degradation by CMZ ternary composite heterojunction.

Keywords Ternary composites · Ofloxacin · ZnO/MoS_2 · CdS/MoS_2 · Photocatalytic degradation

1 Introduction

The use of semiconductors in the photocatalytic degradation of organic wastewater pollutants and water splitting is attracting the attention of the scientists. However, it is difficult to use semiconductors in each application such as the production of hydrogen gas by splitting water, conversion of CO_2, gas sensors, decomposition of organic pollutants [1] etc. To improve the photocatalytic performance of a catalyst that enhances the separation of charge carriers, appropriate co-catalysts can be used [2]. CdS is an II-IV promising semiconductor photocatalysis. Additionally, CdS has high photocatalytic activity and absorb wide range of visible light with narrow band gap [~ 2.2 eV] [3]. However, the oxidation of photo-generated holes, which causes photo-corrosion of CdS, results in poor stability in aqueous solutions [4]. In addition, CdS is an important metal sulfide that provides superior quality hetero composite with MoS_2 [5]. The prepared hybrid structures of Cd based composites enhance the catalytic properties. For example, the homogeneous distribution of catalyst components can be effective in the adsorption and stimulation of active sites. Synergistic effect between components plays a major role in the formation of different electronic arrangements [6]. In crystalline MoS_2, Mo atoms are inserted into two sulfur atom, which is well known as a perfect photocatalyst. It also enhances the photocatalytic performance of co-catalysis. The MoS_2 can be used as an auxiliary catalyst by producing more superoxide radicals [7]. The band gap of MoS_2 varies from 1.3 eV (indirect) to 1.9 eV (direct) [8]. Due to narrow band gap, MoS_2 produces more charge carriers; thus plays a central role to capture light in the CdS/MoS_2 composite [9]. The appropriate band gap position between CdS and MoS_2 accelerates the separation of electron/hole pairs. Recent studies have shown that different morphologies such as nanoparticles, core-shell nanorods and nanosheets of MoS_2/CdS on conductive substrates improve the photocatalytic activity [10]. ZnO is one of the most attractive photocatalyst due to its high photosensitivity, low cost and high electron mobility that make it usable in various energy conversion and photocatalytic systems.

In contrast to the discussion above, there are certain negative aspects in the use of CdS/MoS_2 composites. They have poor electrical conductivity, small surface area (less light

✉ Ali İmran Vaizoğullar
aliimran@mu.edu.tr

[1] Vocational School of Health Care, Medical Laboratory Programme, Muğla Sıtkı Koçman University, 48000 Muğla, Turkey

absorption) and short life of the photo-induced charge carriers [11]. ZnO has higher exciton binding energy, non-toxicity and high electron mobility. However, due to its higher band gap, ZnO can only absorb a small portion of the solar spectrum [12]. Islam et al. [13] have reported higher photocatalytic activity of the hetero dimensional ZnO and MoS_2 nanosheets; attributed to the intimate contact between ZnO and MoS_2 with improved charge transfer and separation of electron/hole pairs. An idea came out to prepare a ternary ZnO/CdS/MoS_2 material where the negative performance of CdS/MoS_2 will be combined with the the efficient catalytic effects of ZnO/MoS_2. Ternary structure with conductive ZnO increases surface area for light absorption and powerful inhibition of electron hole pairs. Since ZnO is piezoelectric material like CdS, highly efficient separation of photo-induced species in the piezo electric field can be obtained [14].

Antibiotics are easily accessible in the twenty-first century. They are playing vital roles in the human as well as animal. Unfortunately, they are used improperly not only in the developing, but also in the developed countries [15]. The by-products of antibiotics, including quinoline-based drugs, though in very low concentrations, are contaminating the environment and causing antibiotic resistant microbes. Therefore, the negative effects of these antibiotic residues should be removed from the environment before they create more pandemic against human beings [16].

In present study, a ternary CdS/MoS_2/ZnO nanomaterial was fabricated with facile chemical precipitation method. However, the synthesis of MoS_2 is novel. The prepared ternary photocatalysts is highly crystalline material with large surface area and wider active sites. Results showed significant photocatalytic and photo electrochemical performance against ofloxacin. Besides, the possible degradation mechanism is also explained with reactive active species.

2 Experimental

2.1 Synthesis of Binary CdS/MoS_2, ZnO/MoS_2 and Ternary CdS/MoS_2/ZnO Samples

Chemical reagents i.e. $Zn(CH_3COO)_2{\cdot}2H_2O$, $Cd(NO_3)_2{\cdot}4H_2O$, Na_2S, NH_3 and NaOH were purchased from Merck (Darmstadt, Germany) and used without further purification. Ethanol, ethylene glycol, sodium thiosulfate pentahydrate ($Na_2S_2O_3{\cdot}5H_2O$), ammonium heptamolybdate tetra hydrate ($NH_4{\cdot}6Mo_7O_{24}$) and ascorbic acid ($C_6H_8O_6$) were purchased from Borkim (Izmir TURKEY). All samples were synthesized using chemical co-precipitation method. To prepare ZnO, 2.36 g of $Zn(CH_3COO)_2{\cdot}2H_2O$ was stirred in a 100 mL beaker. Then 0.1 mol L^{-1} of NH_3 solution was added to prepare Zn $(OH)_2$. The obtained precipitates were filtered and dried at 80 °C and calcined at 300 °C for 120 min. To prepare CdS, 2.58 g NaS was dissolved in methanol/water mixture (30:70 v/v) and into this mixture, 3 mL of ethylene glycol was dropped. The mixture was stirred for 3 h (Solution A). 6.67 g of $Cd(NO_3)_2{\cdot}4H_2O$ was dissolved in 40 mL of water, added into solution A and stirred for 2 h. The obtained precipitates were filtered, centrifuged for 30 min, and dried in an oven at 80 °C for 3 h that revealed CdS. MoS_2 was prepared by dissolving 3.56 g of sodium thiosulfate pentahydrate ($Na_2S_2O_3{\cdot}5H_2O$) into 100 mL of water. Then, 1.25 g of ammonium heptamolybdate tetrahydrate ($NH_4{\cdot}6Mo_7O_{24}$) and 3.47 g of ascorbic acid ($C_6H_8O_6$) was added to the stated solution to obtain Mo^{4+} complex, and into which, 1.98 g of sodium sulfide (Na_2S) was added to precipitate MoS_2. The stoichiometric coefficients were carefully calculated.

CdS/MoS_2: The solubility of CdS and MoS_2 are 8×10^{-28} and 1×10^{-43}, respectively. First, bare MoS_2 was synthesized from Mo^{4+} complex. 2.58 g of Na_2S was dissolved in 50 mL distilled water and slowly added to the above solution followed by the addition of 6.65 g of $Cd(NO_3)_2{\cdot}4H_2O$ and stirred for an hour. The sample was labeled as CM photocatalyst.

ZnO/MoS_2: The solubilities of ZnS and $Zn(OH)_2$ are 2×10^{-25} and 1.2×10^{-17}, respectively. Composite ZnO/MoS_2 was obtained by the precipitation of ZnO and MoS_2. 2.36 g of $Zn(CH_3COO)_2{\cdot}2H_2O$ was dissolved in 50 mL of water and into which, 0.1 mol L^{-1} of NaOH was added to form $Zn(OH)_2$ particles. Molybdenum was first complexed as Mo^{4+} and then precipitated as MoS_2 with 2.5 g of Na_2S. The obtained particles were calcined at 300 °C for 120 min. For ternary sample, 0.25 g of MoS_2 and 2.29 g of Cd $(NO_3)_2$ were stirred in 100 mL of water. Then, 2.256 g of Na_2S was added to this solution to obtain CdS. The obtained yellow-black solids were taken in a 250 mL beaker. To this solution, 1.24 g of $Zn(Ac)_2{\cdot}2H_2O$ was added and stirred for 60 min. Then, 0.1 mol L^{-1} of NaOH solution was dropped to obtain $Zn(OH)_2$ participate. The yellow-black-white precipitates were filtered and washed four times with distilled water and calcined at 300 °C for 120 min. The prepared photocatalysts samples were labelled as CM (CdS/MoS_2), ZC (ZnO/CdS) and CMZ (CdS/MoS_2/ZnO) for photocatalytic and photoelectrochemical performances.

2.2 Characterization

The morphological structure and EDS mapping analysis of the particles was investigated using (SEM) JEOL JSM-7600F). The crystalline structure of the samples was examined by X-ray diffraction (XRD): Rigaku D/MAX 350) using copper K radiation k = 0.154056 nm). X-ray photoelectron spectroscopic (XPS) measurement was performed

using a PHI 5000 Versa Probe. The photoluminescence (PL) emission spectra of the samples were obtained using a spectrofluorometric Spex 500 M, USA). Raman studies were performed at room temperature using Raman spectrophotometer) Bruker IFS 66/S, FRA 106/S, HYPERION 1000, RAMANSCOPE II). The recorded spectra were obtained using 532 nm lasers. The electrochemical impedance spectra) (EIS) were analyzed on an impedance analyzer) Gamry Potansiyostat/Galvanostat/ZRA Reference 3000) using a standard three-electrode system with the samples as the working electrodes, a saturated calomel electrode) (SCE) as the reference electrode, and a Pt wire as the counter electrode. Frequency operating range was specified as 1 kHz–10^7 Hz. The Brunauer Emmett–Teller (BET), surface areas were measured using ASAP2010 (Micromeritics Instrument Corporation, USA) with N_2 adsorption at 77.35 K. The UV–Vis DRS analyses of all the samples were performed using a Lambda 35 UV–vis spectrophotometer in the solid state.

3 Results and Discussion

3.1 SEM Analysis

Figure 1 represents SEM images of bare MoS_2, binary (ZM, CM) and ternary (CMZ) photocatalysts. The morphology of MoS_2 particles was regular with no agglomeration (Fig. 1a). After adding ZnO, polygonal ZnO nanorods and spherical MoS_2 were obtained in clusters (Fig. 1b). The width and length of the ZnO particles were between 500 and 1000 nm. Both travertine-like CdS and spherical MoS_2 were observed in the CM with few elongated crystals that can be attributed to the aggregation of CdS and MoS_2 [17]. When MoS_2, CdS and ZnO particles were combined in the form of ternary CMZ, the dimensions of polygonal ZnO decreased. In addition, MoS_2 is more decorated on cadmium pellets. As known, agglomeration of a particle can be affected by gravitational agglomeration and pH/ionic strength. Therefore, it can be concluded that the gravitation agglomeration is available during the synthesis due to the higher molecular weight of CdS and MoS_2 [18]. The crystal growth mechanism is important future for understanding with high photocatalytic performance. The forming starts with MoS_2 particles which nucleating medium for the next CdS component. However the formation energy of CdS is lower than MoS_2. Many of travertine-like CdS particles reduce surface energy and to form clumps. This results in the agglomeration of MoS_2 onto CdS. When Zn^{2+} ions added to this solution, below reaction occurs; $Zn(CH_3COO)_2 \rightarrow Zn^{2+} + 2CH_3COO$, by adding of NaOH solution, free Zn^{2+} ions react with OH^- to form $Zn(OH)_2$. The growth of ZnO nanorods is the outside from MoS_2/CdS clusters.

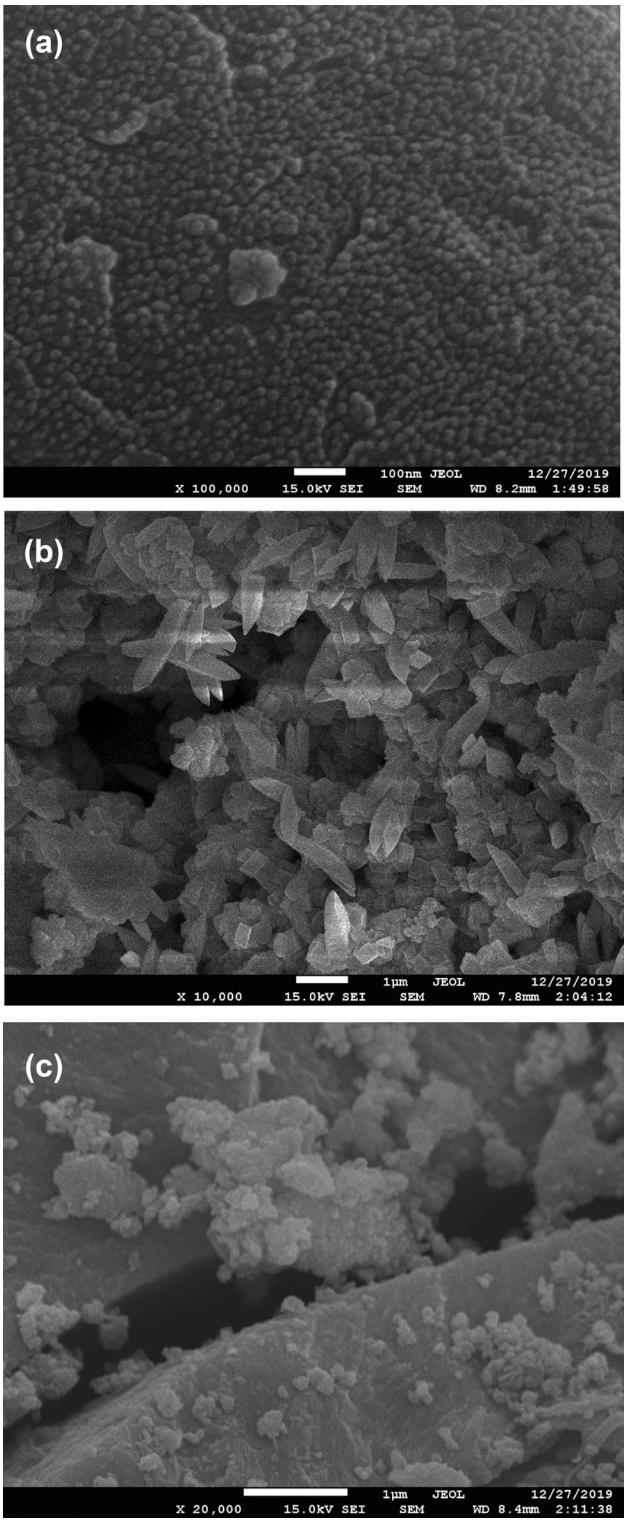

Fig. 1 SEM images of MoS_2 (**a**), ZM (**b**), CM (**c**) and CMZ (**d**); mapping and EDS results of CMZ (**e**) photocatalysts

To further investigate the elemental distribution and composition of CMZ sample, the SEM-EDS mapping analysis was performed (Fig. 1e). The results confirmed a uniform

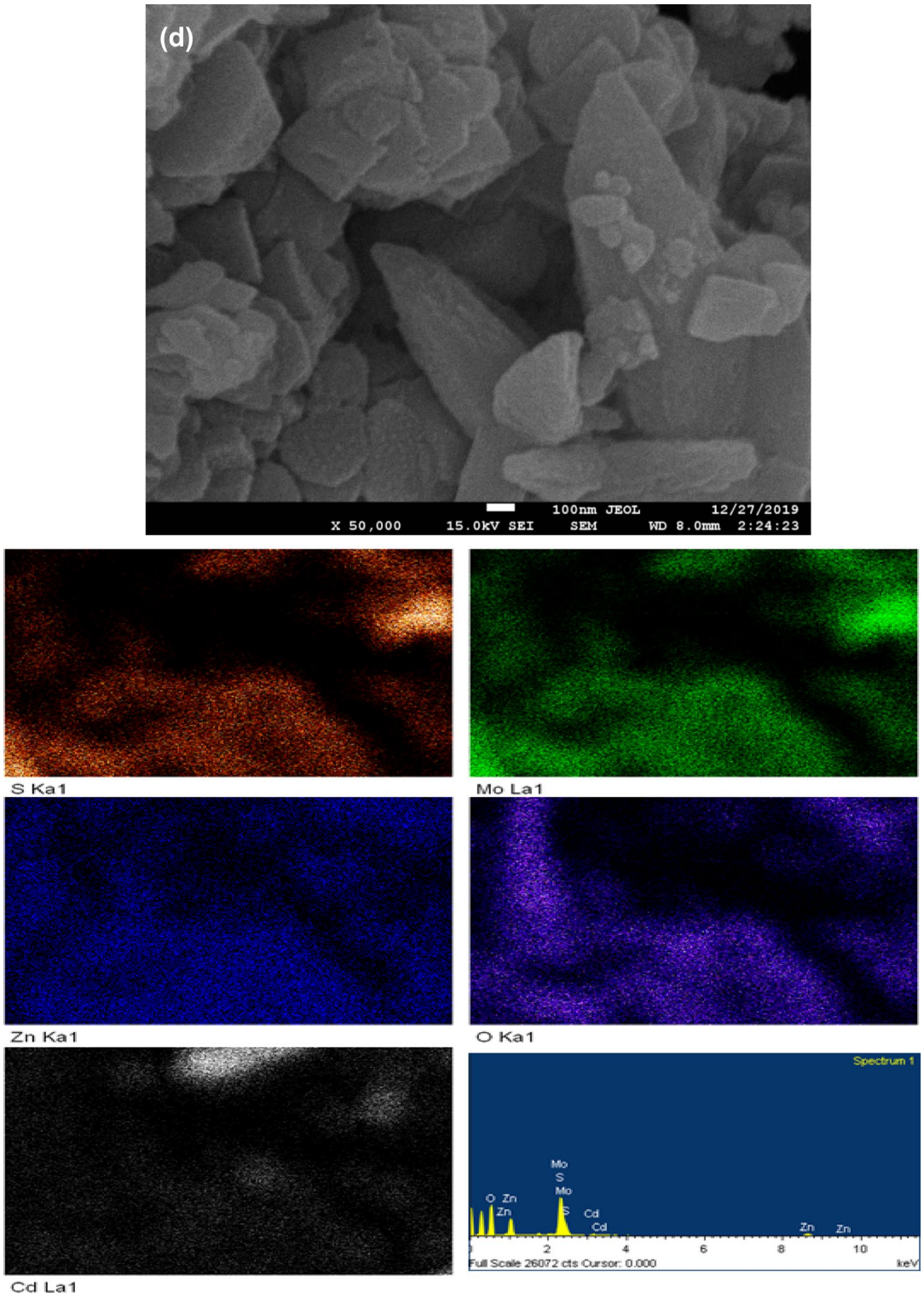

Fig. 1 (continued)

distribution of the elements in the ternary CMZ. The result of the cadmium mapping may be somewhat faint, since the MoS_2 is decorated on CdS. This result coincides with the data in SEM analysis.

3.2 XRD results

Figure 2 shows XRD pattern of bare MoS_2, binary (ZM, CM) and ternary (CMZ) photocatalysts. Pristine MoS_2

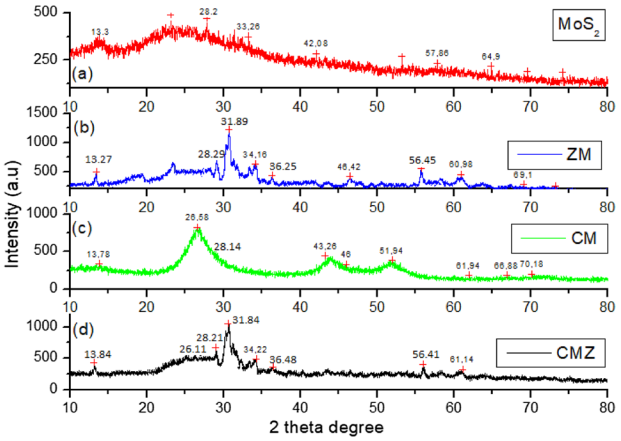

Fig. 2 XRD patterns of the synthesized photocatalysts

exhibits six characteristics 2 theta degree at 13.3°, 28.2°, 33.26°, 42.08° (m40), 57.86° and 64.9° (Fig. 2a) corresponds (002), (004) (100) (103) (110) and (008) plane respectively (JPDS:87-2416). This specifies the hexagonal crystalline structure of MoS_2. For ZM sample, the characteristic ZnO and MoS_2 degrees were also observed (Fig. 2b). In addition to MoS_2 degrees, 31.89°, 34.16°, 36.25°, 46.42°, 56.45°, 60.98° and 69.1° can be attributed to the (100), (002), (101), (102), (110), (103) and (112) planes respectively (JPDS: 89-0510). It is clear that hexagonal ZnO and MoS_2 crystalline structure was obtained. The characteristic peaks of ZnO were not sharper due to the crystalline defect. In addition, the lattice parameters for the ZnO catalyst in the ZM sample are calculated as $a = 0.329$ nm and $c = 0.539$ nm (standard values are $a = 0.326$ nm and $c = 0.522$ nm). The obtained values slightly deviated from the standard values that imply an intra-granular coupling between ZnO and MoS_2 [19]. For binary CM photocatalysts, as the same, both characteristic CdS and MoS_2 2 degrees were observed (Fig. 2c). $2\theta = 26.58°$, 28.15°, 43.26°, 46° and 51.94° degrees relates to (100), (002), (101), (110), (103) and (112) planes respectively. This presents hexagonal crystalline structure of CdS in CM sample. In both binary samples, two characteristic peaks of MoS_2 were slightly observed. Therefore, it can be inferred that the amount of MoS_2 was lower or ZnO and CdS were more dispersed onto other crystallite facets. For ternary CMZ sample, as expected, the characteristic peaks of all three components were observed. These results showed that a composite of all three materials is obtained with no change in their individual crystal structures. In ternary CMZ sample, the main peak of CdS at ~ 26° was reduced due to more dispersed MoS_2 on CdS (supported by SEM images). XRD revealed that the crystallinity growth of MoS_2 is at the [002] facet in CMZ and ZM sample.

3.3 XPS Analysis

XPS spectra were obtained to investigate the chemical composition and valence state of each component in CMZ ternary composite. XPS spectra of CMZ (Fig. 3a) show Zn, Cd, Mo, O, S elements. The peak at 285.6 eV for C 1s attributed to the adventitious carbon from the XPS apparatus. Figure 3b shows three binding energies at 155.67, 161.98 and 167.55 eV, respectively. The XPS peak of 161.98 corresponds to $2p_{3/2}$. Peaks at 155.67 and 167.55 eV were originated from the $S2p_{3/2}$ photoelectrons from different chemical states. The binding energy at 167.55 eV shows the 2p core level energy due to the adsorption site and coverage [20]. In Fig. 3c, the peaks at 405.3, 407.8 and 412.2 eV are typical peaks of Cd^{2+} in CdS for $3d_{5/2}$, $3d_{5/2}$ and $3d_{3/2}$, respectively [15]. The peak at 407.8 eV displays the band bending and shift in valence band structure interface of CMZ [21, 22]. Figure 3d presents XPS results of Molybdenum. Two peaks located at 228.4 and 235.1 correspond to Mo^{4+} $3d_{5/2}$ and Mo^{6+} $3d_{3/2}$ respectively. The Mo^{6+} peak shows the incorporation of oxygen in the MoS_2; since, oxygen can exhibits specific behavior within a crystal structure. For example, it can replace with sulfur sites [23] and bind to Molybdenum at plane edges as an intercalant between basal planes as O_2 or water (H_2O), or as an interfacial Mo-oxide layer due to Mo-oxygen bonding in the ternary composite [24]. In Fig. 3e, the peak of O 1s at 530.9 eV is attributed to O^{2-} in ZnO [25]. The XPS spectrum of Zn 2p reflected two binding energies at 1022.1 and 1045.1 eV for $2p_{3/2}$ and $2p_{1/2}$, respectively (Fig. 3f). Comparison of all XPS results show that the Zn spectra in the CMZ have changed a bit, whereas XPS results for sulfur-based cadmium (Cd) and molybdenum (Mo) showed some differences. These results suggest that there is more intra-granular effect among CdS, MoS_2 and ZnO in the ternary CMZ composite. This will play a significant role in the photocatalytic activity of the ternary sample.

3.4 Raman Analysis

Raman spectra are globally used to investigate the structural characteristics of materials. Figure 4 shows the Raman spectrum of MoS_2 and binary ZM, CM and ternary CMZ. The excitation wavelength is 514.2 nm. Raman spectroscopy is an effective characterization method to reveal spatial structural features of nanocrystals [26]. As seen in Fig. 4a, the characteristic peaks of J2 (219 cm^{-1}), J3 (346 cm^{-1}) are originated from 1T-MoS_2. Peaks at 562 and 485 cm^{-1} display E1 (LO) and edge phonon, respectively [27]. ZnO has longitudinal optical (LO), two modes of E2 phonons and transverse optical (TO). High and low E_2 modes are vibrations of oxygen in the Zn sub lattice [28] while in the case of ZM (Fig. 3b), the peak at 339 cm^{-1} is the second-order Raman spectrum, originating from the zone boundary

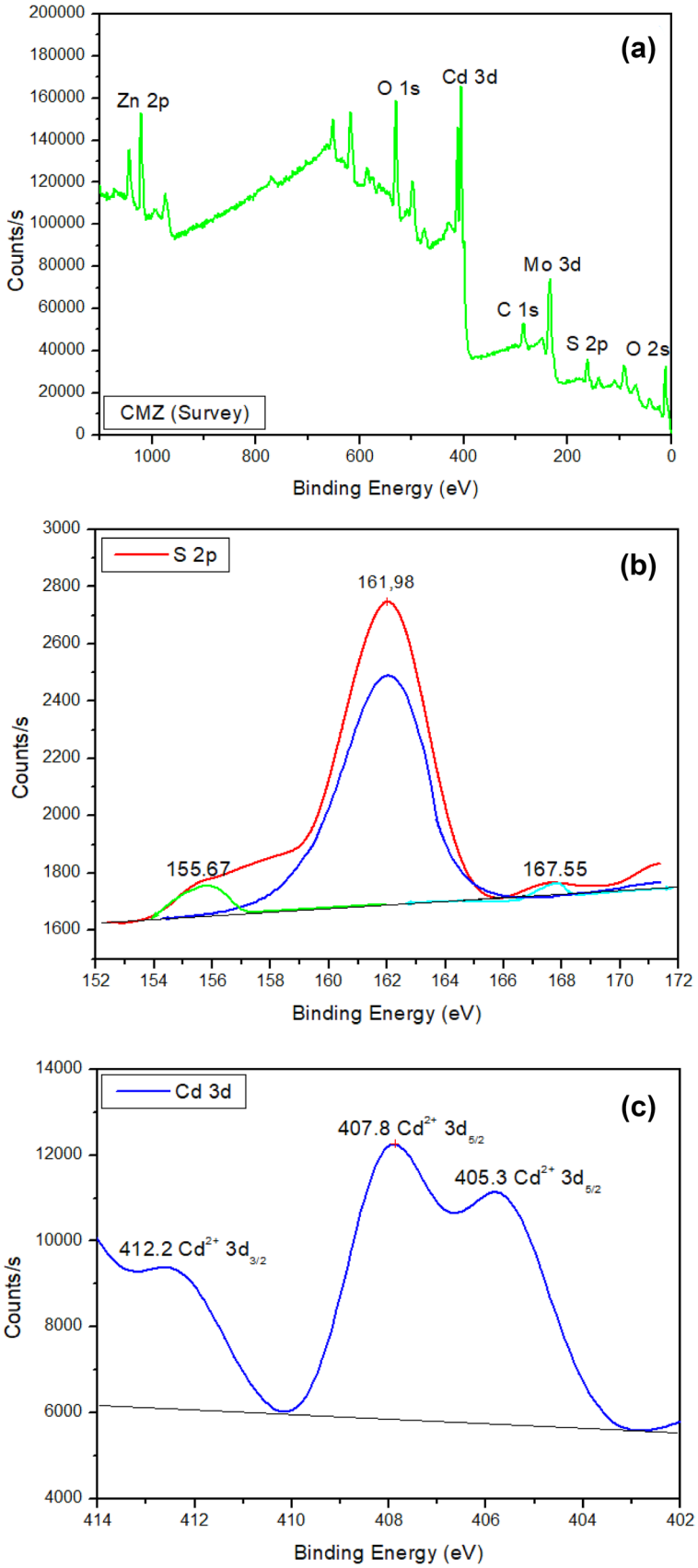

Fig. 3 XPS spectra of **a** survey; **b** S 2p; **c** Cd 3d; **d** Mo 3d; **e** O 1s; **f** Zn 2p

Fig. 3 (continued)

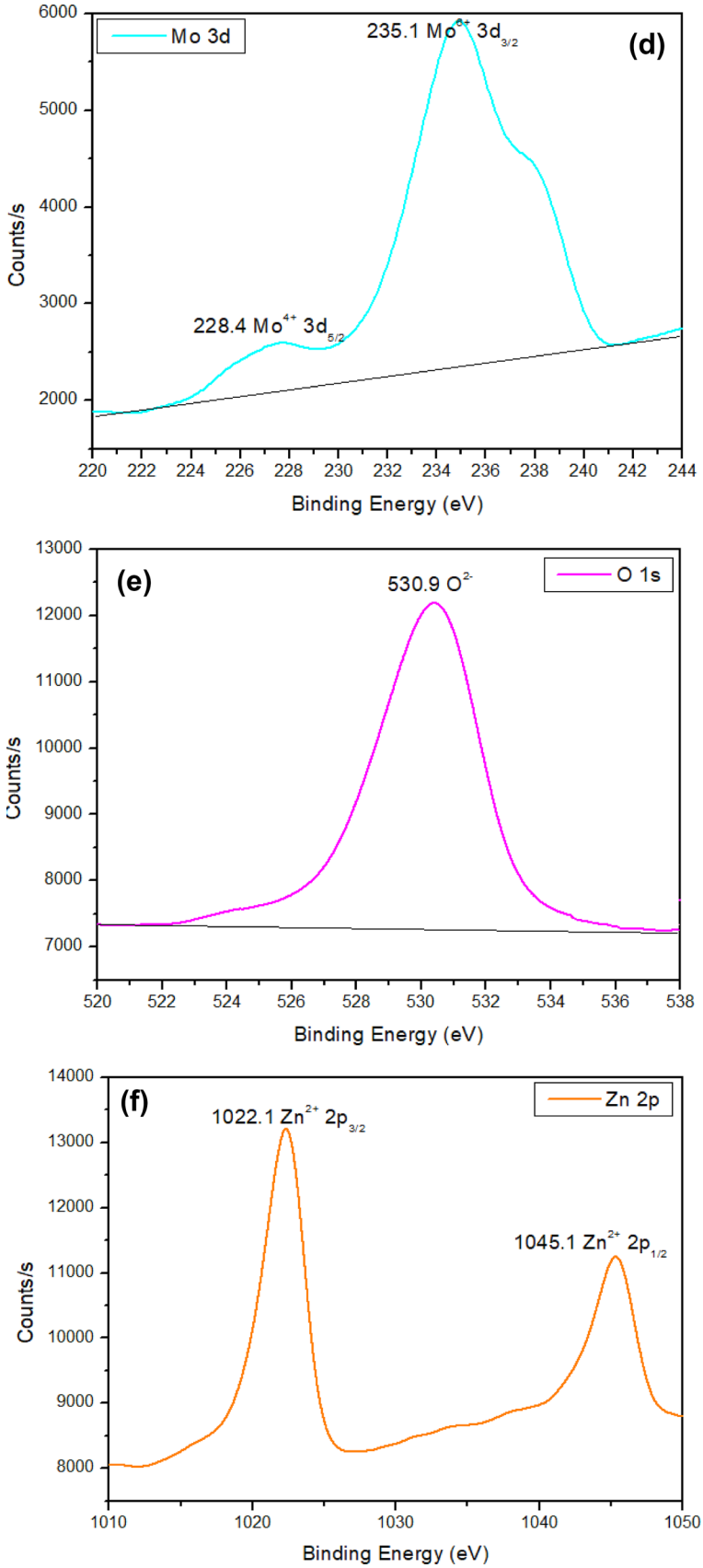

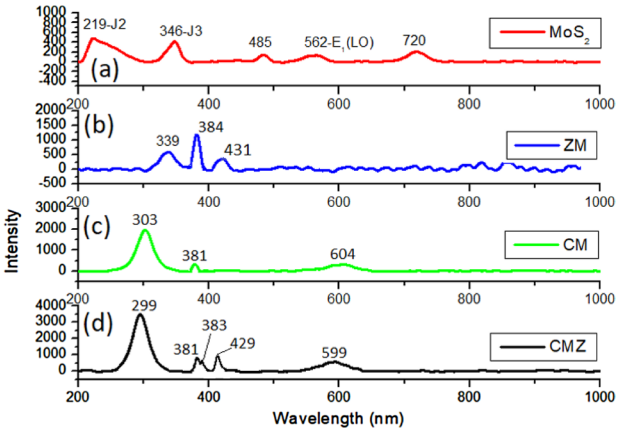

Fig. 4 Raman spectra of all photocatalysts samples

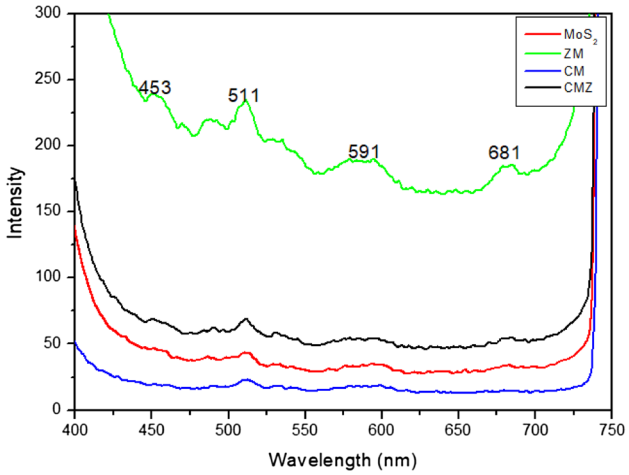

Fig. 5 Photoluminescence spectra of MoS_2, CM, ZM and CMZ excited at the wavelength of 340 nm

phonons $3E_2H–E_2L$. The high E2 mode at 439 cm^{-1} displays band characteristic of wurtzite phase. However, the ZM presented a red shift with 429 cm^{-1}. Thus, the crystallite defects, which are leading to phonon localization or spatial confinement of phonons, causes this shift [29]. This red shift of E_1(TO) in ZM, which shows the presence of MoS_2, could be attributed to impurity and size effect. Figure 4c belongs to the binary CM where the peaks at 303 cm^{-1} and 604 cm^{-1} display 1LO and 2LO modes of CdS [30]. Peak at 381 cm^{-1} represents A1 (TO) of MoS_2. The Comparison of characteristic Raman peaks of CdS and MoS_2 with binary CM (CdS/MoS_2) sample reflects that the vibration modes of CdS are blue shifted (1LO from 300 to 303) and 2LO (from 600 to 604). This is attributed to the electronic interactions of CdS and MoS_2 in CM [31]. The ternary sample shows the Raman peaks of all three components. MoS_2 peak reflected slight shift while CdS and ZnO peaks showed slight red shift. This result is attributed to the electronic interactions and crystal impurities present in the components as mentioned above.

3.5 Photoluminescence Analysis

Photoluminescence analyses have been significantly used to monitor electron and hole pairs to reveal migration, recombination and transfer in a semiconductor material. Photoluminescence results for MoS_2, binary and ternary photocatalysts were recorded at room temperature using excitation wavelength of 340 nm (Fig. 5). As well known, lower PL intensity presents the effective charge separation. However, this is not always the case. The PL spectra of ZM, CM and CMZ composites are similar to that of pure MoS_2 (Fig. 5). Research has shown that multi-layered MoS_2 samples can lead to the reductions in PL intensity. It has also been reported that the multi-layered MoS_2 gives two PL peaks [32]. As shown in Fig. 5, MoS_2 has lower PL intensity and broad emission peaks at 511 and 591, respectively. This indicates that MoS_2 has more layers in ZM, CM and CMZ. The PL of ZM shows four emission peaks at 453, 511, 591 and 681 nm. The peak at 591 nm can be attributed to the trap-related states that generally serve as recombination centers [33]. In addition, the peaks at 453 and 511 nm indicate the oxygen vacancy and zinc interstitial defects in ZM [34]. For ternary CMZ, as seen in Fig. 5, higher PL intensity is obtained. According to these data, we can infer that ternary CMZ has more structural defect. This phenomenon is thought to increase the photocatalytic activity of the ternary structure since the defects in the structure can complicate the recombination of excited electrons. It also indicates catalytic activity in the visible region by changing its optical properties [35].

3.6 UV-DRS Analysis and Electrochemical Impedance

Figure 6 shows UV-DRS spectra of the prepared samples. Generally, the photo-generated holes have powerful oxidation capability with respect to the NHE potential when they have a positive VB maximum. On the other hand, the photogenerated electrons have stronger reduction ability when they have a negative CB minimum. Therefore, for detail explanation, the correct band edge potentials of the semiconductors provide the photocatalytic efficiency. The band edge positions of samples were calculated using the following equations:

$$E_{VB} = \pounds - E_E + 0.5 \times E_g \text{ and } E_{CB} = E_{VB} - E_g,$$

where E_g shows the band gap of each semiconductor (CdS, ZnO and MoS_2) whereas E_E is the free electrons in the hydrogen scale (4.5 eV). E_{VB} and E_{CB} are the VB and CB band edge potentials, respectively while £ is the Mulliken electronegativity of semiconductors. Electronegativity of CdS, ZnO and MoS_2 are 5.19 [36], 5.79 [37] and 5.32 [38],

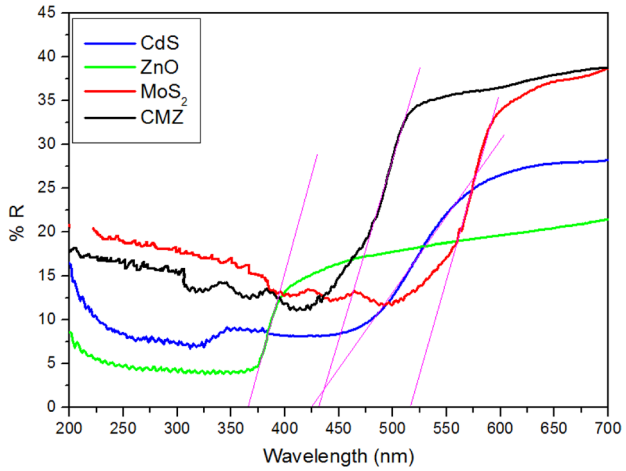

Fig. 6 UV-DRS spectra of bare and CMZ photocatalysts

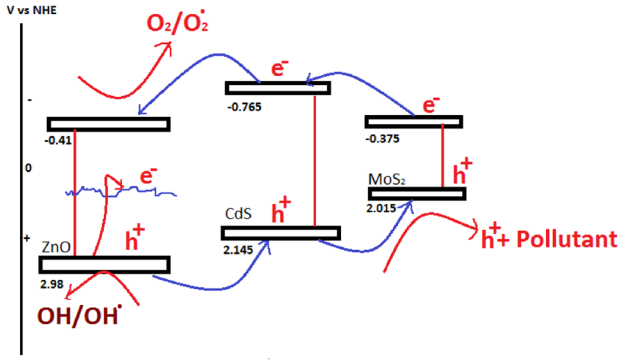

Fig. 7 Schematic diagram of the CMZ ternary photocatalyst

respectively. According to the above equation, the calculated VB and CB band edge potentials of CdS, ZnO and MoS_2 are 2.145, 2.981 and 2.015, and −0.765, −0.41 and −0.375, respectively. The ternary CMZ showed the absorption edge at 432 nm indicating effective visible light absorption for ofloxacin degradation. The obtained optical band gap of CMZ may be either due to the impurity energy levels or many-body interaction occurs in CMZ [39].The photocatalytic degradation mechanism of ternary sample for ofloxacin degradation can be described as below:

$$CMZ + h\vartheta \rightarrow h^+ + e^-$$

$$e^- + O_2 \rightarrow O_2^{-\cdot}$$

$$OH^- + h^+ \rightarrow OH^{\cdot}$$

$$\text{Ofloxacin} + O_2^{\cdot -} \rightarrow \text{Degradation products}$$

$$\text{Ofloxacin} + h^+ \rightarrow \text{Degradation products}$$

$$\text{Ofloxacin} + OH^{\cdot} \rightarrow \text{Degradation products}$$

In a photocatalytic system, first, a photocatalyst should be active in visible region of spectrum. Second, the CB and VB band edge potential of a semiconductor should match with the revealing charge carriers [40]. If a photon absorbs more or equal energy than band gap energy of the semiconductor, the electron and the hole pairs are formed by electrostatic interaction resulting efficient transfer of charge carriers. Third, the photogenerated electron must be effectively separated [41]. When a three-component system is irradiated by visible light, the excited electrons and photogenerated holes can transform into reactive species such as hydroxyl and superoxide radicals. As seen in Fig. 6, the CB band edge potentials of CdS and MoS_2 are more electronegative than that of superoxide radicals, which indicates that formation of super oxide radical in the CMZ ternary sample. Another perspective is that, the excited electrons of MoS_2 can be transferred to CB level of CdS with effective separation of electrons. Also, as stated in the Raman and XRD analysis, the electrons in the VB of ZnO can be induced to a defect level as a result of possible crystal defects occurring in the ZnO structure. The photogenerated holes of ZnO have sufficient potential to form hydroxyl radicals to oxidize ofloxacin. However, since the VB potential of CdS (2.145 eV) is more negative than the standard hydroxyl radical (~2.38 eV vs. NHE), the holes, which transferred to the MoS_2 from CdS, can directly oxidize the organic molecules (Fig. 7). This accelerated charge transportation, reduces the electron-hole

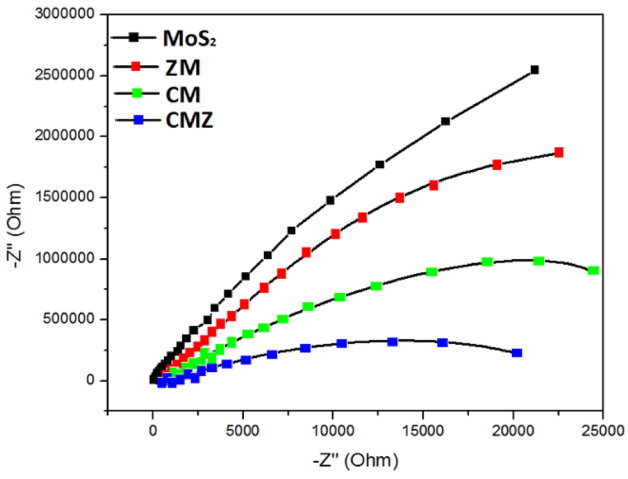

Fig. 8 The electrochemical impedance of photocatalysts (Nyquist plot)

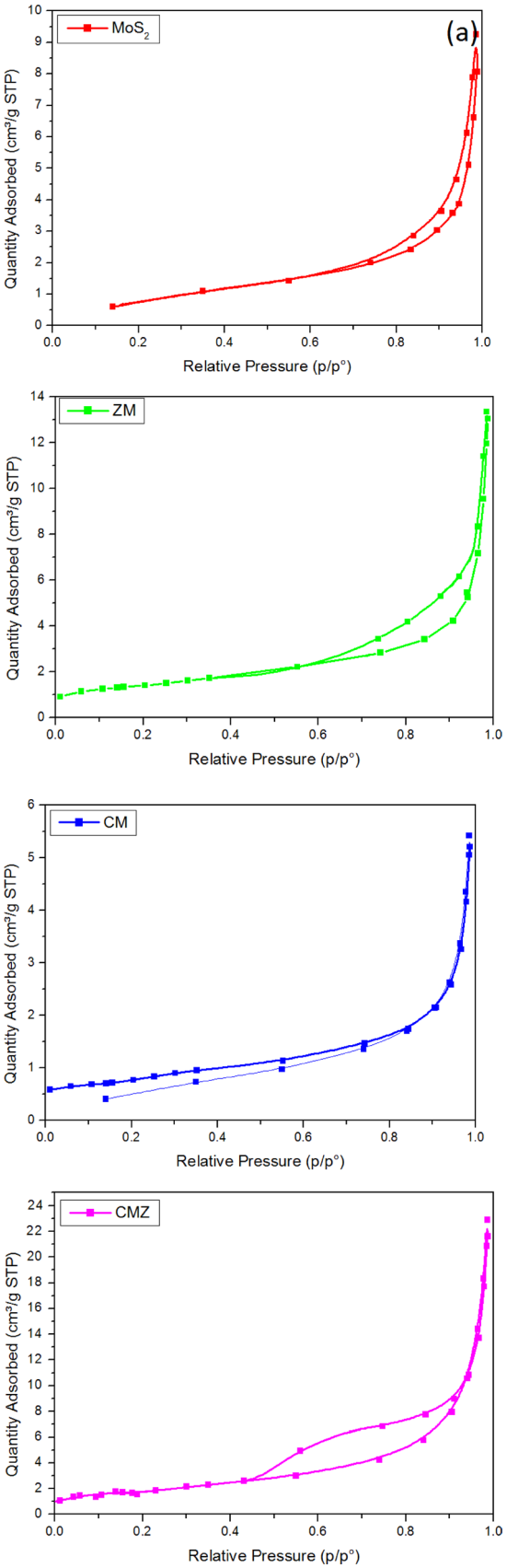

Fig. 9 N_2 adsorption-desorption isotherm of MoS_2, binary ZM, CM ▶ and ternary CMZ samples

recombination, prolonged life-time of charge carriers and trapping at defects located at the interface [42].

The electrochemical impedance was investigated to find out the resistance of charge transfer. As seen in Fig. 8, all samples presented the semicircle diameters. The ternary CMZ exhibited the smallest semicircle arc diameters. Lower arc radius demonstrated the lower resistance and the powerful efficiency of charge separation [43]. A possible explanation for this might be that the ternary system with a p–n CdS/MoS_2 heterojunction and ZnO defects effectively inhibited the charge carries to decompose the ofloxacin antibiotic. Also, it could be assumted that heterogeneity (crystalline defect) does not cause significant qualitative changes in electrochemical impedance spectra. The positive results were due to the synergetic effects of surface plasmon resonance of CdS and defects in the ternary structure. This promotes the faster charge transfer to the photoelectrode surface indicating the photoelectrochemical performance. These results also show the compatibility of the prepared photocatalysts with the photocatalytic activity [44].

3.7 BET Studies

Figure 9 presents the adsorption isotherm of all the photocatalysts. Almost all samples showed Type III isotherm and H3 hysteresis. It means there was unrestricted multilayer adsorption. Comparison of the interaction between catalyst surface and adsorbate, lateral interactions are more dominant between adsorbate molecules. In addition, H3 hysteresis showed plate-like aggregations that formed slit-like pores in the materials. The specific surface area of MoS_2, ZM, CM and CMZ samples were 4.94, 4.95, 2.74 and 16.24 cm^2/g, respectively. The higher surface area of CMZ comes from more active sites that is the reaction center during the photocatalytic activity [45].

3.8 Photocatalytic Performances and Degradation Pathway

The photocatalytic performance of all the samples was evaluated for degradation of ofloxacin antibiotic under visible light irradiation. Photocatalyst sample (0.1 g) was added to the ofloxacin solution (50 mL, 10 ppm) and stirred in dark for 60 min. After light (Xenon lamp, 400 W, $\lambda > 420$ nm) was turned on; aliquots of 2 mL were taken from the reaction device at each 15 min. The taken samples were centrifuged, and forwarded to measure the absorbance in the UV–vis spectrophotometer at 290 nm. The ofloxacin is slightly

soluble in water. However, it has high solubility in glacial acetic acid. Therefore, 0.01 gram of ofloxacin was dissolved in 10 mL of acetic acid. Pure water was added to make the solution at 1000 mL. This solution was used as a stock solution. The photocatalytic activities of samples were studied by decomposing the target molecules by visible light irradiation. Figure 10a represents the photocatalytic degradation activities of all the photocalaysts against the ofloxacin. Ternary CMZ presented the maximum degradation yield that is attributed to the excellent absorption properties of MoS_2 [46]. There was no notable decomposition without catalyst, in dark or visible light, indicating that ofloxacin antibiotic did not decompose by hydrolyses or photolysis. Bare ZnO, MoS_2 and CdS displayed 20, 25.1 and 27.5% decomposition while binary ZM and CM samples showed 52 and 61% degradation percentage in 90 min (Fig. 10a). Therefore, in can be inferred that either charge carrier inhibition of CM sample was higher than that of ZM or lower surface area caused these results. Substantially, 89% of degradation was obtained with ternary CMZ within 90 min. Figure 10b shows the correlation coefficient of all the photocatalyst samples. All reactions followed the pseudo-first order kinetics model as shown by the following equation:

$$\ln\left(\frac{C_0}{C}\right) = k \times t$$

The calculated kinetic rate constant (k) is acquired from the slope that is drawn from the plot of $-\ln(C/C_0)$ versus time. The calculated k values were 0.024 min^{-1} for CMZ sample presenting the highest photocatalytic activity compared to the others. The k value of CMZ ternary composite was approximately 8.5 times higher than the ZnO with the lowest k value and four times higher than CM binary sample with the closest k value. Evaluation of the results discussed shows the highest degradation yield of the ternary composite material results from elongated lifetime of charge carries [47]. The UV–Vis spectra of ofloxacin near the UV region in 90 min degradation by CMZ are shown in Fig. 10c. The absorption peak of ofloxacin gradually decreased with the increasing of irradiation time. It reached 89% degradation yield within 90 min. This result shows that the ternary material has a strong ability without any oxidative substance in the aqueous medium, and an efficient degradation occurred.

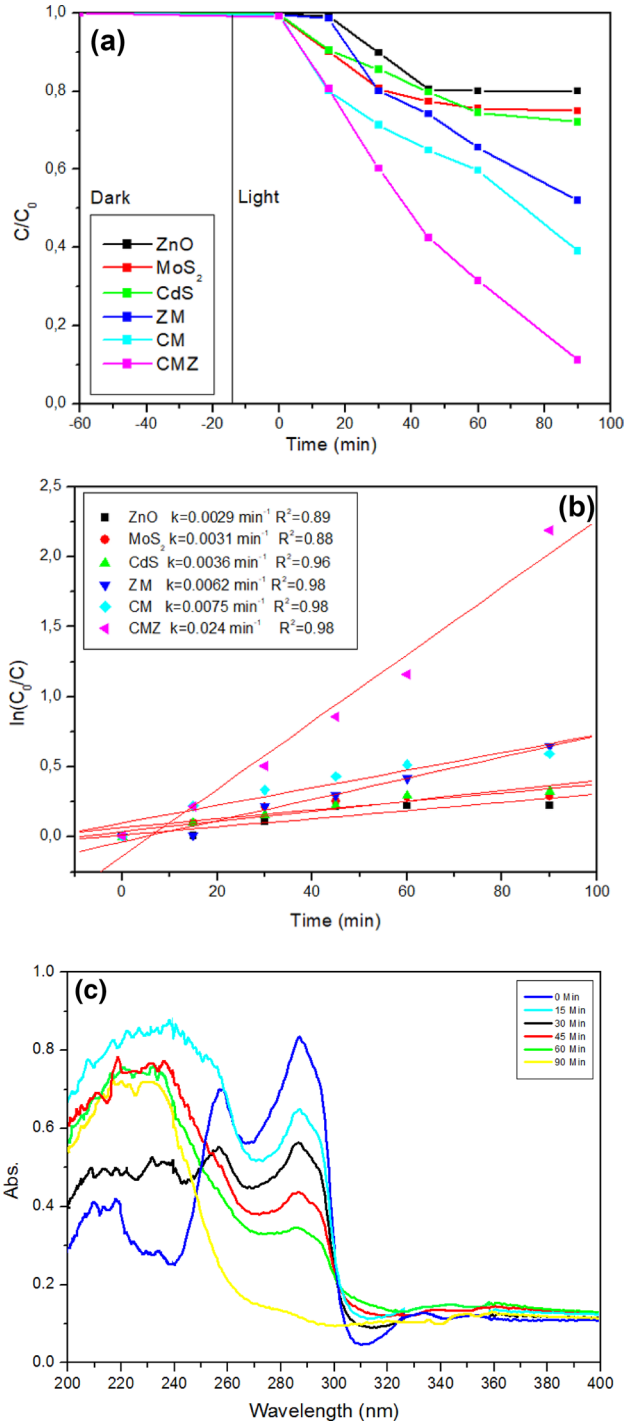

Fig. 10 Photocatalytic degradation of all photocatalysts: **a** the degradation performance of all catalysts sample; **b** pseudo first order kinetic rate; **c** UV–Vis spectra of ofloxacin within 90 min

3.9 Quantum Yield (QY)

As well known, higher inhibition of electron hole pairs in the heterogeneous photocatalyst shows higher QY. The QY values of photocatalysts were calculated using the following formula:

$$QY = \frac{\text{Rate of disapperiance of reactant molecules}}{\text{Rate of incident photons}} = \frac{k_{app} \times C_0}{I} = \frac{k_{app} \times C_0 \times \text{Energy}(eV)}{W}$$

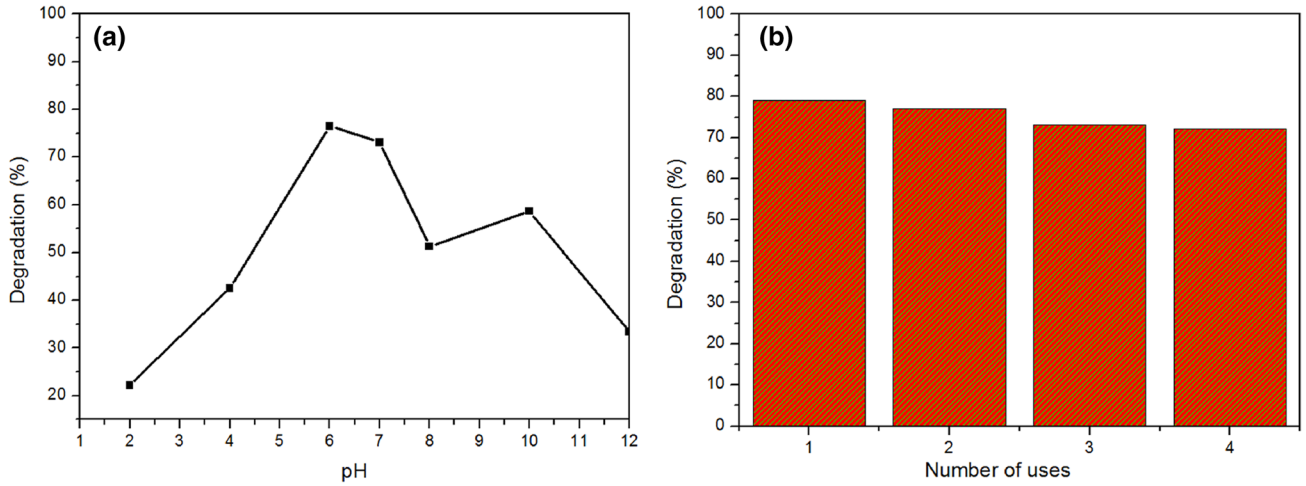

Fig. 11 The effect of pH on ofloxacin degradation and recyclable of CMZ

where k_{app} is the first-order kinetic rate constant of photocatalysts, C_0 is the initial ofloxacin concentration and I is the intensity of incident photons [48]. In all photocatalytic experiments (except for the kinetic rate constant), C_0 and I were the same. The obtained QY for six photocatalysts sample were in the range of 21.4×10^{-4}–17.7×10^{-4} under the same conditions. This indicates that the combination of ternary CMZ sample can provide a new feasible approach for the effective photocatalytic studies in the near future.

3.10 Effect of pH and Recyclable Performance

The pH effect was evaluated in terms of both ofloxacin and CMZ catalyst. Since the catalyst consists of three different components, the isoelectric point (IEP) was measured, which was 6.4 while that of ofloxacin was 4.4. Degradation studies at different pH performed are given in Fig. 11. In fact, it is very difficult to explain how the pH effect occurs since electrostatic interactions occur between the catalyst and substrate in addition to the radicals appearing during the reaction [49]. The degradation efficiency increased with the solution pH up to 7.2 and then dropped afterwards. As known, the surface charge of a catalyst is positive below the isoelectric point and negatively above it. As seen from Fig. 11a, the degradation yield of CMZ did not increase until the pH 4, then gave a peak between 4 and 7, and finally dropped. At pH 7, the degradation yield remained constant; may be due to the decrease of the ofloxacin solubility at that pH [50]. When pH started to increase, since the surface charges of both the catalyst and ofloxacin were the same, the degradation efficiency decreased. Interestingly, the degradation yield increased at pH 10 and then decreased. These inconsistencies can be based on some sulfur-induced electro-kinetic effects such as photoirradiation, lattice defects surface oxidation etc. [51]. Figure 11b shows the catalytic perfromance of CMZ ternary photocatalyst after four uses. As seen from the figure, a slightly change in the photocatalytic performance was observed indicating a good ternary photocatalyst for degradation studies.

4 Conclusions

Ternary CMZ photocatalyst, and binary CM and ZM samples were produced successfully using chemical precipitation and complexation. The ternary CMZ sample degraded 89% ofloxacin antibiotic in 90 min upon visible light irradiation. The enhanced photoelectrochemical and photocatalytic performances can be connected to the prolonged charge carriers, defect levels and possible surface plasmon resonance. This study adds several contributions to the current literature. First, literature emphasis on the higher photocatalytic activity of binary materials. However, the ternary composite prepared in this study showed higher photodegradation as compared to the binary composites. Results obtained in this study suggest a light to explore further the synthesis methods, structural properties and illuminating the band structures. Second, MoS_2 synthesis method with chemical precipitation was used for the first time in this study. Finally, this is the first study of ternary $CdS/MoS_2/ZnO$ composite for photocatalytic degradation. This study was limited by the deeper understanding of interaction in CMZ ternary composite system. Further studies are needed to improve the morphology (core shell, 3D, wire etc.) of these ternary composites and their usage in the water treatment or decomposition of organic compounds.

Acknowledgements This work was supported by Muğla Sıtkı Koçman University Coordination of Scientific Research Project Unit with 19/088/01/1/1.

References

1. K.R. Reddy, M. Hassan, V.G. Gomes, Appl. Catal. A **489**, 1–16 (2015)
2. Y. Zhong, Y. Shao, F. Ma, Y. Wu, B. Huang, X. Hao, Nano Energy **31**, 84–89 (2017)
3. A. Nezamzadeh-Ejhieh, Z. Banan, Desalination **284**, 157–166 (2012)
4. R. Marschall, Adv. Funct. Mater. **24**(17), 2421–2440 (2014)
5. Y. Liu, Y.X. Yu, W.D. Zhang, J. Phys. Chem. **117**(25), 12949–12957 (2013)
6. R. Koutavarapu, C.V. Reddy, B. Babu, K.R. Reddy, M. Cho, J.Shim, Int. J. Hydrogen Energ. **45**(13), 7716–7740 (2020)
7. M. Xu, J. Zhao, Electron. Mater. Lett. **14**(4), 499–504 (2018)
8. W. Shin, H.J.Y. Son, Electron. Mater.Lett. **14**(1)), 59–63 (2018)
9. W. Kim, M. Seol, H. Kim, J.B. Miller, A.J. Gellman, K. Yong, J. Mater. Chem. A **1**(34), 9587–9589 (2013)
10. J. Ji, L. Guo, Q. Li, F. Wang, Z. Li, J. Liu, Int. J. Hydrogen Energ. **40**(10), 3813–3821 (2015)
11. Y. Tang, Z. Zheng, X. Sun, X. Li, L. Li, Chem. Eng. J. **368**, 448–458 (2019)
12. S. Kumar, V. Maivizhikannan, J. Drews, V.Krishnan, Vacuum **163**, 88–98 (2019)
13. S.E. Islam, D.R. Hang, C.H. Chen, K.H. Sharma, Chem. Eur. J. **24**(37), 9305–9315 (2018)
14. D.Q. Zheng, Z. Zhao, R. Huang, J. Nie, L. Li, Y.Zhang, Nano Energy **32**, 448–453 (2017)
15. Z. Shi, J. Liu, H. Lan, X. Li, B. Zhu, J. Yang, J. Mater. Sci. Mater. Electron. **30**(19), 17682–17692 (2019)
16. R. Dhabbe, A. Kadam, P. Korake, M. Kokate, P. Waghmare, K. Garadkar, J. Mater. Sci. Mater. Electron. **26**(1), 554–563 (2015)
17. U. Krishnan, M. Kaur, G. Kaur, K. Singh, A.R. Dogra, M. Kumar, Mater. Res. Bull. **111**, 212–221 (2019)
18. A. Singer, Z. Barakat, S. Mohapatra, S.S. Mohapatra, Nanoscale drug-delivery systems: in vitro and in vivo characterization, in *Nanocarriers for Drug Delivery*. ed. by S.S. Mohapatra, S. Ranjan, N. Dasgupta, R.K. Mishra, S. Thomas (Elsevier, Amsterdam, 2019), pp. 395–419
19. S. Zhang, F. Tang, J. Liu, W. Che, H. Su, W. Liu, Radiat. Phys. Chem. **137**, 104–107 (2017)
20. J. Jia, A. Kara, L. Pasquali, A. Bendounan, F. Sirotti, V.A. Esaulov, J. Chem. Phys. **143**(10), 104702 (2015)
21. S. Velanganni, S. Pravinraj, P. Immanuel, R.Thiruneelakandan, Physica B **534**, 56–62 (2018)
22. K.K. Liu, W. Zhang, Y.H. Lee, Y.C. Lin, M.T. Chang, C.Y. Su, …C.S. Lai, Nano Lett. **12**(3), 1538–1544 (2012)
23. J.R. Lince, M.R. Hilton, A.S. Bommannavar, Surf. Coat. Technol. **43**, 640–651 (1990)
24. S. Hussain, J. Singh, D. Vikraman, A.K. Singh, M.Z. Iqbal, M.F. Khan, J. Eom, Sci. Rep. **6**(1), 1–13 (2016)
25. C.V. Reddy, I.N. Reddy, B. Akkinepally, K.R. Reddy, J. Shim, J. Alloys Compd. **814**, 152349 (2020)
26. B.C. Windom, W.G. Sawyer, D.W. Hahn, Tribol. Lett. **42**(3), 301–310 (2011)
27. Y. Zhang, S. Guo, X. Xin, Y. Song, L. Yang, B. Wang, Appl. Surf. Sci. **504**, 144291 (2020)
28. N. Ashkenov, B.N. Mbenkum, C. Bundesmann, V. Riede, M. Lorenz, D. Spemann, E.M. Kaidashev, A. Kasic, M. Schubert, M. Grundmann, G. Wagner, H. Neumann, J. Appl. Phys. **93**(1), 126–133 (2003)
29. A. Khan, J. Pak. Mater. Soc. **4**(1), 5 (2010)
30. Z. Zhang, Y. Dong, G. Liu, J. Li, H. Sun, H. Luo, S. Liu, Colloids Surf. A Physicochem. Eng. Asp. **589**, 124431 (2020)
31. M.B. Ali, W.K. Jo, H. Elhouichet, Int. J Hydrogen Energ. **42**(26), 16449–16458 (2017)
32. J.W. Park, H.S. So, S. Kim, S.H. Choi, H. Lee, J. Lee, Y. Kim, J. Appl. Phys. **116**(18), 183509 (2014)
33. Y. Liu, H. Niu, W. Gu, X. Cai, B. Mao, D. Li, Chem. Eng. J. **339**, 117–124 (2018)
34. S. Kumar, V. Maivizhikannan, Vacuum **163**, 88–98 (2019)
35. A. Vaizoğullar, J. Mater. Sci. Mater. Electron. **29**(15), 13292–13301 (2018)
36. R. Rajendran, K. Varadharajan, V. Jayaraman, B. Singaram, J. Jeyaram, Appl. Nanosci. **8**(1–2), 61–78 (2018)
37. M. Basu, N. Garg, A.K. Ganguli, J. Mater. Chem. A **2**(20), 7517–7525 (2014)
38. X. Cui, X. Yang, X. Xian, L. Tian, H. Tang, Front. Chem. **6**, 123 (2018)
39. C.V. Reddy, I.N. Reddy, V.V.N. Harish, K.R. Reddy, N.P. Shetti, J. Shim, T.M. Aminabhavi, Chemosphere **239**, 124766 (2020)
40. A. Mishra, A. Mehta, S. Basu, N.P. Shetti, K.R. Reddy, T.M. Aminabhavi, Carbon **149**, 693–721 (2019)
41. A. Mehta, A. Mishra, S. Basu, N.P. Shetti, K.R. Reddy, T.A. Saleh, T.M. Aminabhavi, J. Environ. Manag. **250**, 109486 (2019)
42. V.N. Rao, N.L. Reddy, M.M. Kumari, P. Ravi, M. Sathish, K.M. Kuruvilla, M.V. Shankar, Appl. Catal. B Environ. **254**, 174–185 (2019)
43. S.K. Balasingam, J.S. Lee, Dalton Trans. **44**, 15491–15498 (2015)
44. S.P. Vattikuti, I.L. Ngo, C.Byon, Physicochemcial characteristic of CdS-anchored porous WS_2 hybrid in the photocatalytic degradation of crystal violet under UV and visible light irradiation. Solid State Sci. **61**, 121–130 (2016)
45. C.V. Reddy, I.N. Reddy, B. Akkinepally, V.V.N. Harish, K.R. Reddy, S. Jaesool, Ceram. Int. **45**(12), 15298–15306 (2019)
46. K.K. Paul, N. Sreekanth, R.K. Biroju, T.N. Narayanan, P.K. Giri, Sol. Energy Mater. Sol. Cells **185**, 364–374 (2018)
47. K. Saravanakumar, G. Mamba, V. Muthuraj, Colloid Surf. A **581**, 123845 (2019)
48. W.A. Sadik, A.G.M. El-Demerdash, A.W. Nashed, A.A. Mostafa, H.A. Hamad, J. Mater. Res. Technol. **8**(6), 5405–5414 (2019)
49. P.Y. Motlagh, A. Khataee, T.S. Rad, A. Hassani, J. Taiwan Inst. Chem. E **101**, 186–203 (2019)
50. I. Michael, E. Hapeshi, C. Michael, D. Fatta-Kassinos, Water Res. **44**(18), 5450–5462 (2010)
51. L. Reyes-Bozo, M. Escudey, E. Vyhmeister, P. Higueras, A. Godoy-Faúndez, J.L. Salazar, R. Herrera-Urbina, Miner. Eng. **78**, 128–135 (2015)